



3D bioprinted breast tumor-stroma models for pre-clinical drug testing

Patricia González-Callejo^{a,1,**}, Paula Vázquez-Aristizabal^{a,b,1}, Clara García-Astrain^{a,c},
Dorleta Jimenez de Aberasturi^{a,c,d}, Malou Henriksen-Lacey^{a,c}, Ander Izeta^b,
Luis M. Liz-Marzán^{a,c,d,*}

^a CIC BiomaGUNE, Basque Research and Technology Alliance (BRTA), 20014, Donostia-San Sebastián, Spain

^b Biodonostia Health Research Institute, Tissue Engineering Group, Paseo Dr. Beguiristain s/n, 20014, Donostia-San Sebastián, Spain

^c Centro de Investigación Biomédica en Red, Bioingeniería, Biomateriales y Nanomedicina (CIBER-BBN), 20014, Donostia-San Sebastián, Spain

^d Ikerbasque, Basque Foundation for Science, 48009, Bilbao, Spain

ARTICLE INFO

Keywords:

3D bioprinting
Bioinks
dECM
Breast cancer
Tumor microenvironment
3D tumor models
Drug testing

ABSTRACT

The use of three-dimensional (3D) bioprinting has been proposed for the reproducible production of 3D disease models that can be used for high-throughput drug testing and personalized medicine. However, most such models insufficiently reproduce the features and environment of real tumors. We report the development of bioprinted *in vitro* 3D tumor models for breast cancer, which physically and biochemically mimic important aspects of the native tumor microenvironment, designed to study therapeutic efficacy. By combining a mix of breast decellularized extracellular matrix and methacrylated hyaluronic acid with tumor-derived cells and non-cancerous stromal cells of biological relevance to breast cancer, we show that biological signaling pathways involved in tumor progression can be replicated in a carefully designed tumor-stroma environment. Finally, we demonstrate proof-of-concept application of these models as a reproducible platform for investigating therapeutic responses to commonly used chemotherapeutic agents.

1. Introduction

Breast cancer remains a significant global health burden, with a high mortality rate for women, mainly due to inter-patient variations in prognosis, response to therapy, and clinical outcomes [1,2]. Among different tumor subtypes, triple-negative breast cancer (TNBC) is considered to be highly aggressive and heterogeneous, due to the lack of hormone receptor (HR) expression, basal-like cell phenotype, and genetic diversity. These factors enhance the challenge of developing effective treatments for this subtype of breast cancer [3]. Therefore, the development of prognostic preclinical *in vitro* models capable of mimicking tumor physiology would provide an interesting opportunity to identifying the most suitable treatment regimens for individual patients in a personalized manner [4–6].

Patient-derived three-dimensional (3D) tumor organoids have shown promise as a tool for the development of personalized treatments [7]. Compared to traditional two-dimensional (2D) cell culture systems, organoids have various benefits, such as improved preservation of tissue

architecture and cellular interactions, as well as the capability to replicate the tumor's response to drugs. However, organoids often do not capture the complexity of the tumor microenvironment (TME) [8], which is a major challenge in the development of complex 3D *in vitro* models [9].

Breast tumors evolve in a complex niche, where the tumor cells core is surrounded and infiltrated by various types of stromal and immune cells, embedded within the extracellular matrix (ECM) [10]. The TME is characterized by a complex bidirectional communication network established between cancer cells, stromal cells, and ECM components, which is difficult to recreate in an artificial *in vitro* environment [11].

In this context, 3D bioprinting has shown promise toward creating realistic tissue models, by assembling various cell types and biomaterials with high spatial resolution [12]. This technology provides a means to recreate the tumor complexity, as well as its functional and structural hierarchies, for an accurate study of tumor growth, response to treatment, and other aspects of cancer biology [13,14]. 3D bioprinting can be used to create personalized tumor models that mimic the specific

* Corresponding author. CIC BiomaGUNE, Basque Research and Technology Alliance (BRTA), 20014, Donostia-San Sebastián, Spain.

** Corresponding author.

E-mail addresses: pgonzalez@cicbiomagune.es (P. González-Callejo), llizmarzan@cicbiomagune.es (L.M. Liz-Marzán).

¹ Patricia González-Callejo and Paula Vázquez-Aristizabal contributed equally to this work.

characteristics of a patient's cancer, potentially leading to the development of individualized treatment plans or evaluation of drug candidates at *in vitro* lab settings [15–17].

An essential component of 3D-printed organoids are bioinks, which must provide the mechanical properties necessary for cell adhesion, proliferation, and differentiation [18–20]. Common bioinks include natural and synthetic polymers and hydrogels, chosen on the basis of their mechanical stability and simplicity of processing. However, when used to recreate the tumor ECM, they have several drawbacks such as a lack of biological relevance and poor cell-matrix interactions [21]. An interesting alternative involves the use of decellularized extracellular matrices (dECMs), obtained by removing all cellular components from the tissue source. dECMs can better mimic the native biological and physiological ECM environment and crucially do not include immunostimulatory nucleic acids and tumor-stimulatory factors, which are often encountered in tumor-derived ECMs such as Matrigel [22,23]. Additionally, bioprinted tumor models often lack a proper representation of the TME and its cellular heterogeneity [24–28].

We report herein the development of a 3D-bioprinted breast tumor-stroma model that mimics some of the complexity of breast tumors, including the tumor architecture, the location of tumoral and stromal cells, and the ECM signaling cues that make up the breast TME. Cells of relevance to the TME (human TNBC MDA-MB-231 tumor cells, stromal breast fibroblasts (HBF), and endothelial cells (EC)) are combined with a porcine breast tissue-derived dECM bioink and organized into a tumor core-stroma structure that closely resembles the architecture of breast carcinomas. Our 3D-bioprinted model can efficiently express several biomarkers associated with TNBC tumor biology, including the epithelial-to-mesenchymal transition (EMT) pathway, cancer stem cells (CSC), cancer-associated fibroblasts (CAFs), and the typical cytokine secretion pattern of the activated TNBC TME. We additionally investigated the potential of this model as a preclinical drug testing platform. We therefore generated an additional MCF-7 bioprinted tumor-stroma model, to determine variations in targeted therapy response between HR-expressing and TNBC tumor-stroma subtype models. Our results show that the MCF-7 3D model responds to Tamoxifen targeted therapy, whereas the TNBC MDA-MB-231 model is only slightly sensitive to the same drug. These findings reflect clinical responses typically observed in patients, thereby highlighting the value of bioprinted models toward testing the use of targeted therapies on tumor cells. The present study thus provides an *in vitro* platform that can be used to investigate tumor progression and therapeutic response, toward the development of more effective treatments for breast cancer.

2. Materials and methods

2.1. ECM decellularization and bioink formulation

Porcine breast tissue was obtained from the slaughterhouse and stored at -80°C until needed. The entire breast tissue was utilized to create the dECM formulation, thawed in a water bath at 37°C , minced into 1 cm^3 cubes, frozen in liquid nitrogen and thawed again. The tissue was decellularized according to Mollica et al. with slight modifications [29]. Briefly, after exposing the tissue to 0.5% (w/v) SDS, a treatment of 40 U/mL Denarase from *S. marcescens* (activity: 296U/ μL ; purity $\geq 99\%$) at 37°C overnight was performed. Denarase is specialized for breaking the phosphodiester bonds connecting nucleotides, resulting in the formation of shorter fragments consisting of approximately 3–5 base pairs and displaying its activity on both DNA and RNA, single-stranded and double-stranded configurations, linear and circular structures, as well as those that are supercoiled, enabling a simpler, more efficient process. To enhance solubility and optical characteristics, the tissue was subjected to a delipidation step with absolute isopropanol (IPA) and acetone. The dECM was sterilized with 0.1% (v/v) peracetic acid (PAA) and 4% (v/v) ethanol (EtOH) for 2 h and subsequently washed twice with PBS and twice with distilled water. Freeze-drying for 72 h was carried out to later

grind the dECM to powder. The bioink (dECM) was obtained by digesting 25 mg of dECM powder per mL of 1 mg/mL pepsin in 0.5 M acetic acid solution for 48 h. The pH was neutralized to pH 7.4 on ice and later diluted with DMEM supplemented with 10% (v/v) fetal bovine serum (FBS) to a final concentration of 20 mg/mL (2% w/v). A summary table of the protocols is available as [Supplementary Table 1](#).

2.2. Histology of the ECM and dECM

The tissues were fixed in Histofix overnight at 4°C , washed thrice in PBS and left overnight in 30% (w/v) sucrose solution at 4°C , prior to embedding them in OCT tissue freezing medium. Frozen blocks were stored at -80°C until needed. $7\text{ }\mu\text{m}$ tissue sections were stained with $1\text{ }\mu\text{g/mL}$ DAPI for 30 min after re-hydration and permeabilizing the tissue with 0.3% (v/v) Triton X-100 for 30 min and mounted in Fluoromount-G. Hematoxylin/Eosin staining protocols were optimized for each tissue and mounted in DPX. Cryo-sections of $7\text{ }\mu\text{m}$ were hydrated in water and submerged in propylene glycol for 2 min. Subsequently, tissue sections were stained with Oil Red O and developed with 85% (v/v) propylene glycol for 1 min for delipidation evaluation. Prior to mounting in Mowiol 4–88, 2 washings with distilled water were performed.

2.3. DNA quantification

5 mg of each tissue was digested in 500 μL of digestion buffer (100 mM Tris, 2 mM EDTA, 150 mM NaCl, 1% (w/v) SDS, and 200 $\mu\text{g/mL}$ of proteinase K) for 48 h at 56°C . DNA was manually precipitated with ethanol as described in Green et al. [30] Double stranded DNA in both ECM and dECM was analyzed with a Quant-iT PicoGreen dsDNA assay kit following the manufacturer instructions and including calf thymus DNA in $1\times$ Tris-EDTA buffer as a standard. Samples in 96-well plates were excited at 492 nm and emission was recorded at 535 nm in an Appliskan microplate reader.

2.4. Proteomic analysis

Samples were processed by the Proteomic Platform Service at CIC bioGUNE (Derio, Spain) for the relative quantification of the peptides by label free LC-MS/MS, following the protocol described by Wisniewski et al. [31] with minor modifications, and analyzed in a hybrid trapped ion mobility spectrometry – quadrupole time of flight mass spectrometer (timsTOF Pro with PASEF, Bruker Daltonics) coupled online to a nano-Elute liquid chromatograph (Bruker). Protein identification and quantification were carried out using MaxQuant software with default settings [32]. Searches were carried out against a database consisting of pig protein entries (Uniprot/Swissprot + TrEMBL), with precursor and fragment tolerances of 20 ppm and 0.05 Da. Only proteins identified with at least two peptides at FDR $<1\%$ were considered for further analysis. Intracellular and membrane proteins were discarded, and only ECM-related proteins were plotted and analyzed according to MatrisomeDB [33].

2.5. Rheological characterization

Measurements for assessing rheological properties of cell-free bioinks were performed on a MCR302 rheometer (Anton Paar) equipped with a 25 mm diameter cone/plate and parallel plate geometries, and a Peltier plate. A humidity chamber was used to keep the samples hydrated during the measurements and excess material was trimmed before the start of any measurement. The gap for measurements was adjusted to the type of sample analyzed in each case. Amplitude sweeps were performed to determine the linear viscoelastic region, where both the storage (G') and loss (G'') moduli are independent of frequency (Figs. S2 and S7). Frequency sweeps of the cross-linked samples were performed at constant amplitude (0.15% for dECM, 0.005% for cross-linked dECM, and 0.05% for HAMA/dECM), previously determined

from the amplitude sweeps and at constant temperature: 37 °C for cross-linked gels, 10 °C for dECM. For the dECM ink, a temperature ramp was performed from 10 to 40 °C at constant frequency (1 Hz) and a heating rate of 1 °C/min. Flow curves were also performed from 0.1 to 1000 s⁻¹ to monitor the viscosity of the material at 10 °C.

2.6. Scanning electron microscopy

dECM/HAMA bioinks were cross-linked for 5 s under UV light. Samples were freeze-dried before coating them with a thin gold/palladium layer by magnetron sputtering and then imaged with a JSM-6490LV microscope (JEOL), with a working distance of 10 mm and 15 kV acceleration voltage.

2.7. Cell culture

Primary human breast fibroblasts (HBF) were purchased from Innoprot (Derio, Spain) and human breast MDA-MB-231 and MCF-7 cell lines were obtained from American Type Culture Collection (ATCC, HTB-26 and HTB-22, respectively). These cell lines were cultured in DMEM supplemented with 10% FBS with 1% penicillin/streptomycin (Fisher Scientific). Human aortic endothelial cells (TeloHAEC) were purchased from the ATCC and cultured in vascular cell basal medium (VCBM) supplemented with Endothelial Cell Growth Kit-VEGF (ATCC; PCS-100-030, PCS-100-041). All cell lines cultures were grown in standard tissue culture conditions at 37 °C with 5% CO₂.

2.8. Cytotoxicity tests

The cytotoxicity of dECM on HBF, MDA-MB-231, MCF-7, and ECs was estimated by a lactate dehydrogenase (LDH) assay kit (CyQuant assay, ThermoFisher). Cells were seeded at a density of 5,000 cell/cm² on 96-well plates and the cross-linked dECM was incubated overnight with DMEM supplemented with 10% FBS, according to the ISO-10993-5:2009, to obtain the extractive medium. 24 h later the seeding, medium was replaced with the conditioned medium and incubated for additional 24 h. Cell medium (50 µL) was transferred to an optically clear 96-well plate and mixed with reaction buffer (50 µL) for 30 min, prior to addition of stop reactant and measurement of the absorbance at 490 nm and 680 nm. All measurements were performed in triplicates at different time points.

2.9. Biocompatibility of dECM gels

To assess cell viability within the dECM bioink, cells were mixed with the dECM bioink at a concentration of 5 × 10⁵ cells/mL, seeded in Ibidi 8-well plates, and maintained in culture for 5 days. Then, cell viability was monitored using a live/dead cell assay. 3D cell cultures were incubated with Calcein AM (1/100) and PI (1/50) for 20 min. The corresponding confocal images were analyzed and the percentage of live cells was quantified and represented as the number of live cells with respect to the number of total cells using ImageJ software. To assess cell proliferation within the dECM cultures, cells were prelabelled with CellTracker™ Green CMFDA Dye, CellTracker™ Deep Red, or CellTracker™ Blue CMF₂HC Dye (ThermoFisher) before embedding them in the dECM 3D culture, and maintained for 7 days. Confocal images were acquired at different timepoints and the total fluorescence intensity of 3 random image sections was measured using ImageJ software. Cell proliferation for each cell population was assessed by normalizing fluorescence intensity of images acquired at day 7 related to fluorescence intensity displayed at day 1.

2.10. dECM/HAMA bioink formulation

Hyaluronic acid (HA) was functionalized with methacrylate groups. HA (hyaluronic acid sodium salt from *Streptococcus equi* (MW ≈

1.5–1.8 × 10⁶ Da) (500 mg) was dissolved in 50 mL of Milli-Q-water and the pH of the solution was adjusted to 8 using 0.5 M NaOH, while keeping the solution in ice. Then, methacrylic anhydride was added in 20-fold excess under continuous stirring and the pH was readjusted to 8. After 24 h of reaction at room temperature, the reaction was stopped, and the mixture precipitated in 500 mL of ethanol. The resulting precipitate was filtrated and dialyzed against water using cellulose dialysis membranes (MW cut-off 14 kDa), to remove the unreacted reagent. Methacrylated hyaluronic acid (HAMA) was recovered after freeze-drying. The degree of methacrylation was estimated by ¹H NMR by comparing the integration of the signals of the methyl groups around 1.8 ppm with the ones corresponding to the methylene group at 6 and 5.6 ppm, resulting in a degree of methacrylation of 75%. Lyophilized HAMA was mixed with the dECM at a final concentration of 2% (w/v) and with Irgacure photoinitiator (0.1% w/v) and stored at 4 °C until use.

2.11. Bioprinting of 3D tumor model

A multi-headed 3D Discovery bioprinter (RegenHU, Switzerland) equipped with a biosafety cabinet was used. MDA-MB-231 cells prelabelled with CellTracker™ Green CMFDA Dye were mixed with the dECM/HAMA bioink at a 1.5 × 10⁷ cells/mL concentration. Tumor cores were printed as 4-layered circular structures with a printing design of 1 mm in diameter in Ibidi 8-well chamber slides (Ibidi). Bioinks were extruded through a dispensing stainless steel needle with an internal diameter of 0.3 mm (Nordson) at 10 °C, pressures of 0.06–0.08 MPa, and speeds of 4–6 mm/s. The constructs were then cross-linked by UV light (365 nm, output power of 500 mW) for 20 s and placed in a cell incubator for 15 min at 37 °C. Resulting tumor constructs had dimensions of 2.5 mm in diameter and 1 mm in height. Cell media was then added to the well plates and 3D tumor models were maintained under standard culture conditions.

2.12. Bioprinting of tumor-stroma model

The tumor compartment of the constructs comprised 100% MCF-7 or MDA-MB-231 cells. The stromal compartment comprised 50% HBF and 50% EC (cell number ratio). Prior to bioprinting, cells were fluorescently labeled with different fluorescent cell trackers (CellTracker™, ThermoFisher). Cancer cells were stained with CellTracker™ Green CMFDA Dye, HBFs with CellTracker™ Deep Red, and ECs with CellTracker™ Blue CMF₂HC Dye. For the tumor compartment, cancer cells were mixed in the dECM/HAMA bioink at a 1.5 × 10⁷ cells/mL and printed as previously described. For the stromal compartment, HBF and EC were mixed in the appropriate proportions in the dECM ink at a concentration of 1 × 10⁷ cells/mL. The stromal compartment was printed surrounding the tumor core compartment as a 4-layered circular structure of 2 mm diameter. The 1 cm² well served as the container before the matrix was cross-linked by heating. dECM bioinks were extruded through a dispensing needle with an internal diameter of 0.3 mm (Nordson) at 10 °C, pressures of 0.010–0.012 MPa, and printing speeds of 0.5–1 mm/s. Immediately following bioprinting, tumor-stroma models were placed at 37 °C to promote dECM bioink cross-linking. Resulting tumor-stroma constructs measured 1 cm × 1 cm × 3 mm. After 20 min, a 50:50 mix of supplemented DMEM and VCBM was added to the culture plates. Constructs were then incubated for up to 7 days.

2.13. 3D model imaging

All confocal images were recorded in a Zeiss LSM 880 confocal laser scanning microscope, equipped with 405 nm (blue fluorophore excitation), 488 nm (green fluorophore excitation) and 633 nm (far red fluorophore excitation) lasers, and Plan-Apochromat 10 × (0.45 N.A.) and Plan-Apochromat 20 × (0.8 N.A.) objectives. In the case of 3D characterization of tumor models, Z-stacks (ca. 50 µm thick) were obtained, and a post-imaging maximum intensity projection (MIP) filter was

applied.

2.14. Viability of 3D models

Cell survival in the bioprinted tumor and tumor-stroma models was evaluated with live/dead staining assay. 3D models were incubated with Calcein AM (1/100) and PI (1/50) for 20 min. Resulting confocal images were analyzed using ImageJ software.

2.15. Histological analysis of the tumor-stroma model

For histological analysis, tissues were fixed in 4% paraformaldehyde (Electron Microscopy Sciences, Hatfield, PA) for 20 min at 37 °C and left overnight in 30% (w/v) sucrose solution at 4 °C, prior to embedding them in OCT tissue freezing medium. Frozen blocks were stored at -80 °C until needed. Tissue sections (7 µm) were stained with Hematoxylin/Eosin and mounted in DPX.

2.16. Immunofluorescence assays

For immunofluorescence images, 3D tumor-stroma models were washed twice with PBS, fixed with paraformaldehyde 4% (20 min, RT), permeabilized with 0.5% Triton X-100 (20 min, RT), and blocked with 2% BSA + 0.1% Triton X-100 in PBS overnight. 3D models were then incubated with primary antibodies for 3 days (1:50, 4 °C), washed and incubated with secondary antibodies for 48 h, (1:500, 4 °C), and DAPI (20 min, RT). The list of antibodies is detailed in Table S2. Immunofluorescence images were acquired on a Zeiss LSM 880 confocal microscope with Zen software (Zeiss Microscopy) and image analysis was performed using ImageJ software.

2.17. Cytokine profiling

Proteome Profiler Human XL Cytokine Array assays (R&D Systems, ARY022B) were performed according to the manufacturer's protocol. In brief, culture supernatants from cross-linked dECM, and two biological replicates of bioprinted 3D tumor, stroma, and tumor-stroma models, were collected and added to the array membranes, incubating overnight at 4 °C. Membranes were washed, incubated with a streptavidin-HRP-coupled antibody (1:2000) for 30 min at RT and developed using Chemi-Reagent Mix. Images were captured and visualized using the LICOR Odyssey Fc imaging system and dot integrated densities were measured using ImageJ software. Integrated density was calculated as the product of the area of a selected region of interest (ROI) and its mean pixel intensity. ROI areas were manually selected by drawing a region around each dot of the membrane. Further, each sample's dots integrated density values were normalized to each membrane's control dots integrated density. Original membranes images are depicted in Fig. S14.

2.18. Drug treatment and therapeutic response studies

Doxorubicin, Paclitaxel and Tamoxifen were purchased from Merck (Original stocks: Tamoxifen 50 mM in DMSO with 1% methanol, Paclitaxel 1.17 mM in milli-Q water, and Doxorubicin 1.8 mM in milli-Q water). MCF-7 and MDA-MB-231 tumor models were sequentially bioprinted in a 48-well high-throughput testing plate and then exposed to increasing concentrations of Tamoxifen, Paclitaxel or Doxorubicin for 72 h. Control groups were non-treated cells cultured with complete media. Cell media was collected, and drug cytotoxicity was measured using the LDH assay according to manufacturer instructions. Data shown in graphs are the summary of a minimum of three biological replicates in three independent experiments. LDH assays data were normalized to negative (control) and positive (Triton-X 100) cell death controls. Resulting dose-response curves were calculated using GraphPad Prism software through non-linear regression analysis.

2.19. Statistical analysis

Bar graphs and point graphs display mean value ± SEM. Statistical analysis consisted of normality data distribution assessment by the Kolmogorov-Smirnov test. Data fitting into a normal distribution was submitted to unpaired Student's *t*-test, for single comparison of means, or one-way ANOVA for multiple comparisons. Otherwise, nonparametric Bonferroni's test was employed for multiple mean comparisons. The significance threshold was established at $P < 0.05$, and significance levels were schematically assigned $*(0.01 \leq P < 0.05)$, $** (0.001 \leq P < 0.01)$, $*** (0.0001 \leq P)$. All analyses and graphs were performed using GraphPad Prism 6 software (GraphPad, San Diego, CA).

2.20. Schemes and cartoons

Schemes and cartoons were produced with [Biorender.com](https://biorender.com) (License agreement number: ZK255JNUOL).

3. Results and discussion

3.1. dECM ink production and characterization

Creating a biologically and physiologically accurate environment that mimics the native breast ECM is crucial for developing efficient *in vitro* breast tumor models. We chose to work with porcine breast tissue due to its abundance, similarity with human breast tissue regarding ECM composition, and biocompatibility with human-derived cells [34]. We thus proceeded to decellularize and delipidate porcine breast tissue, using a protocol adapted from Mollica et al. [29], and described in detail in the Supporting Information (SI) Table S1. A schematic illustration of the dECM bioink production process is provided as Fig. S1. To assess the effectiveness of the decellularization process, we performed histological analysis to evaluate and compare the presence of cells and lipids within the native ECM and the dECM (Fig. 1A). The histological examination demonstrated that the dECM preserved the general structure of the original ECM yet being free of cellular material, as demonstrated by Hematoxylin and Eosin (H&E), as well as DAPI staining. In addition, the dECM displayed a significant decrease in lipid content as compared to the native ECM, which was confirmed by Oil Red O staining. Histological staining methods were also employed to assess both collagen and glycosaminoglycan distribution (Fig. S2). To further assess the residual DNA content in the dECM, DNA quantification analysis was conducted. As shown in Fig. 1B, the dECM contained significantly less DNA compared to the ECM samples, indicating that the decellularization process met common acceptance criteria (<50 ng/mg tissue) [35]. The dECM was subsequently ground into a powder, digested under acidic conditions, and finally the pH neutralized to produce the dECM bioink.

To evaluate the gelation properties of the bioink, we conducted rheological tests monitoring the storage (G') and loss (G'') moduli of the samples within a temperature range from 10 up to 40 °C (Fig. 1C). At lower temperatures, G'' was over G' , indicating liquid-type behavior. However, as the temperature increased, both G' and G'' increased as a consequence of the thermal cross-linking of collagen in the samples and G' started surpassing G'' at approximately 25 °C, which pointed out the start of gelation. Above 30 °C, both moduli increased significantly, showing a typical gel-like behavior that was monitored over time at constant temperature (37 °C) and reached a maximum value after ca. 5 min (Fig. S3). Frequency sweeps recorded before and after cross-linking showed the characteristic gel-like behavior as G' was greater than G'' in the linear viscoelastic region. Both values were higher for the cross-linked samples and had a similar modulus to that of the native tissue [36]. The resemblance of the dECM moduli to the native breast tissue ensures an adequate 3D milieu for breast tissue-derived cell culture because it replicates the natural microenvironment. The gelation process was also compatible with the bioprinting approach, as the material could be extruded at lower temperatures and cross-linked after printing

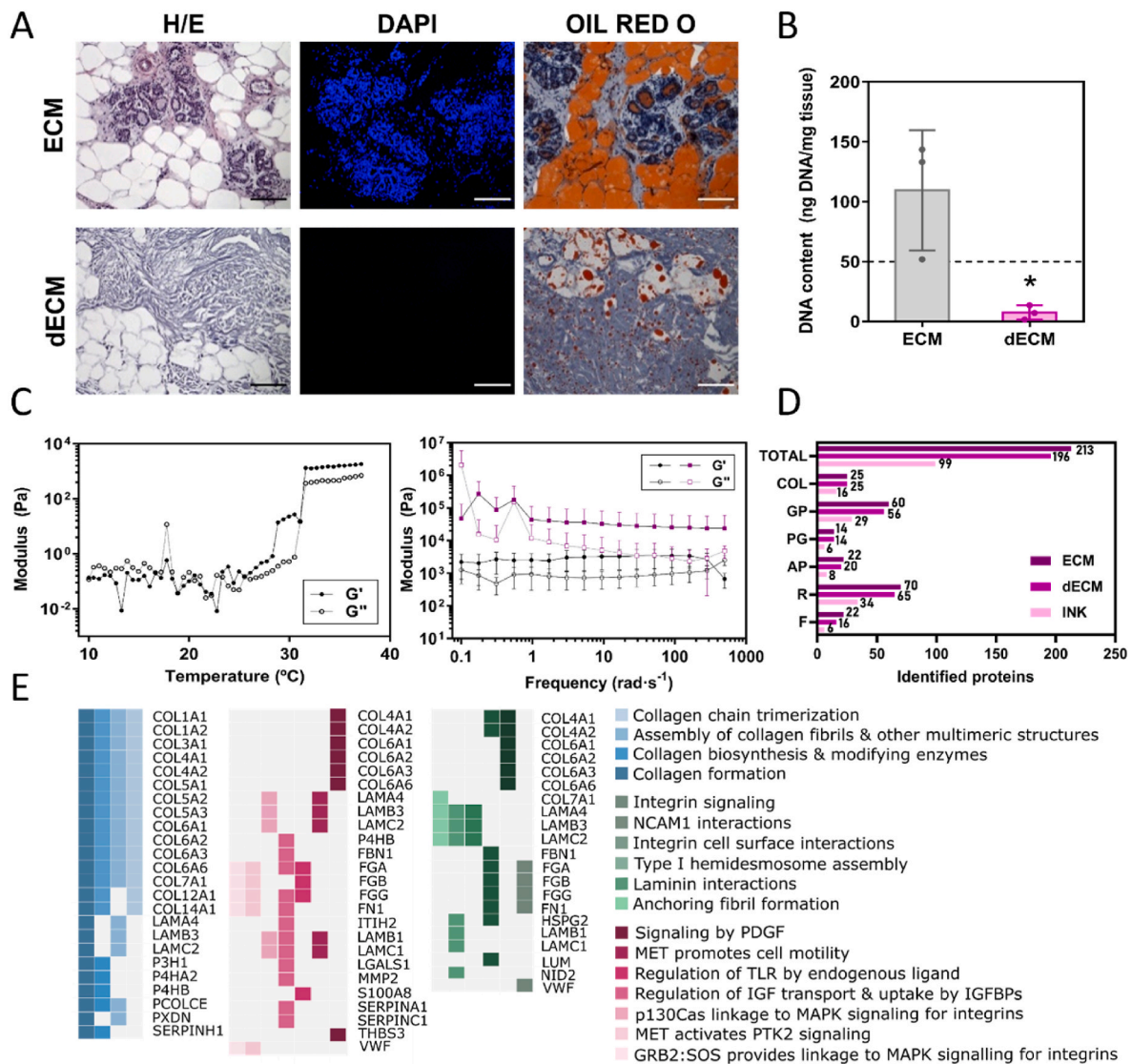


Fig. 1. dECM production and characterization. (A) Histological analysis of ECM/dECM, showing the tissue structure by H&E staining (left), nuclei by DAPI (center) and delipidation by Oil Red O (right) staining. Scale bars: 150 μ m. (B) DNA content of ECM and remnant DNA in dECM after decellularization treatments. Threshold for acceptance criterion set at 50 ng/mg. (C) Rheological characterization including temperature ramp and frequency sweep tests of the dECM ink before (black) and after cross-linking (purple). (D) Quantification of the number of proteins identified by LC-MS/MS in the native ECM, dECM and dECM ink. (E) Classification by function of the identified proteins within the dECM matrisome (blue, synthesis and assembly of collagenous fibers; green, ECM organization and cell/ECM interaction molecules; pink, cell signaling and regulation).

under mild temperatures. These rheological studies revealed the compatibility of the bioink with extrusion printing, under conditions compatible with cell viability.

Contrary to other conventional materials used for bioink formulations (e.g., gelatin, collagen, and alginate) containing a single natural component, dECMs have a more complex biochemical composition. The proteins contained in this molecular network are responsible for the ECM assembly itself, but they also have an influence on cellular processes such as adhesion, differentiation, growth, and signal transduction. Precisely one of the main drawbacks of 2D cultures, regarding correlation with *in vivo* systems, is the absence of the matrix biochemical and physical cues. Hence, to assess the similarity of the developed bioink to the original tissue composition, we conducted a thorough liquid chromatography–mass spectrometry (LC-MS/MS) analysis of the peptides present in the original breast tissue ECM, dECM, and dECM bioink (Fig. 1D). The results suggest that the total number of identified proteins was reduced by half during the entire bioink processing (213 vs. 99 in the ECM vs. dECM vs. dECM bioink), albeit with few changes in the

number of collagens or proteoglycans. The major proteomic loss from dECM to dECM bioink can be attributed to the acidic digestion of the dECM powder with pepsin, which cleaves phenylalanine-phenylalanine and phenylalanine-tyrosine bonds. The exact proportion of each ECM component in all three materials is represented in Fig. S4. The list of the genes coding for the identified proteins was submitted to ENRICH, classified on the basis of their function, and plotted according to their main contribution in cellular biology (Fig. 1E) [37]. Most of the identified proteins were related to collagen formation, assembly and trimerization, in addition to cell-matrix interactions, platelet-derived growth factor (PDGF) signaling, and neural cell adhesion molecule (NCAM1) interactions [38–40]. Many other proteins involved in ECM organization and cell adhesion were also identified, such as von Willebrand factor (VWF), fibronectin, fibrinogen, and lumican, all of which are key for integrin function and known to promote endothelial and epithelial cell adhesion [38,41,42]. Different laminins present in the dECM matrix are known to contribute to hemidesmosome formation, and hence, to cell attachment, cell movement and maintenance of phenotype, but also to

c-MET/integrin complex-related signal transduction [43]. Proteins such as P4HB, FBN1, fibrinogens, fibronectin, LGALS1, serpins, or MMP2 were found to be related to insulin-like growth factor (IGF) signaling [42,44–46]. Some of these proteins are also related to MAPK or FAK (PTK2) signaling cascades, which are relevant in tumorigenesis because they determine cell proliferation, locomotion and spreading processes [47–50]. Overall, the presence of such signaling molecules and other components in the final dECM bioink supports its use as a biologically relevant ECM over other materials such as collagen hydrogels or Matrigel. One notable advantage is their ability to provide a highly customizable and natural environment for cells retaining not only the native biochemical but also the biophysical properties of the source tissue. In addition, dECM hydrogels have been shown to have better long-term stability compared to Matrigel, which is usually degraded by cells. However, the preparation of dECM-derived hydrogels can be a complex and time-consuming process, which may limit their widespread use. Nonetheless, their potential advantages over other commonly used hydrogels highlight the importance of considering the specific needs and goals of the research when selecting a biomaterial for certain

applications.

3.2. dECM supports cells viability and proliferation

Upon confirmation that the dECM bioink retains multiple biological signaling cues from the original ECM tissue, we aimed at studying the dECM-based bioink biocompatibility. We selected the TNBC cell line MDA-MB-231, together with stromal cells that are typically found in breast tissue, namely HBFs and ECs. HBFs represent the most abundant non-neoplastic stromal cell type within breast tumors, whereas ECs play an important role in the supply of nutrients [51]. To study any possible cytotoxic effects from components that may leach from our dECM bioink, the lactate dehydrogenase (LDH) cytotoxicity assay was applied to cells cultured in contact with the dECM bioink. We observed that the dECM exerted background levels of cytotoxicity on all three cell populations, after 72 h in culture. Notably, EC displayed reduced levels of cytotoxicity compared to the control. This observation suggests that the soluble factors secreted by dECM into the media might foster EC growth and viability, as compared to the control media. (Fig. 2A). To assess cell

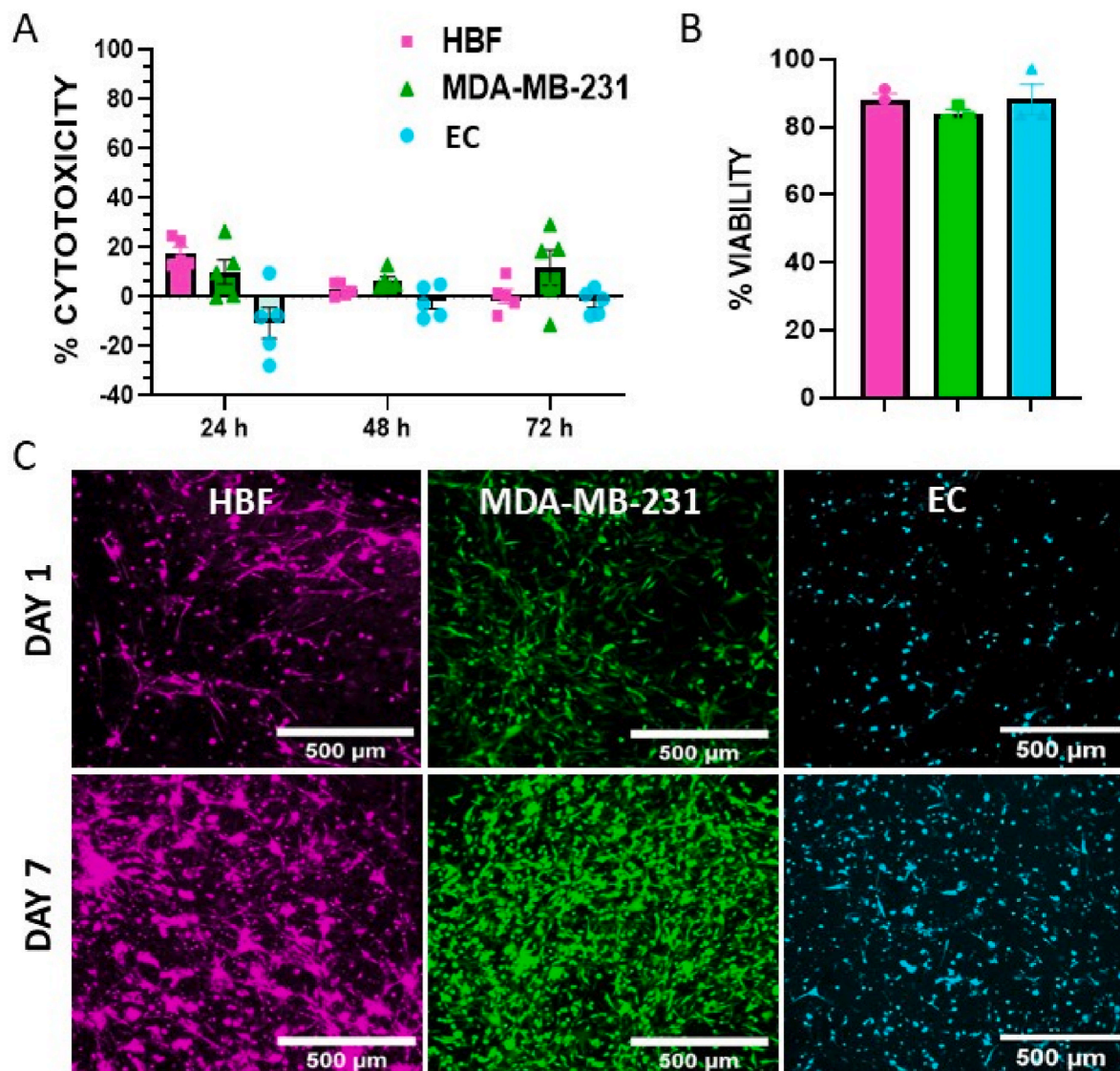


Fig. 2. Evaluation of dECM bioink biocompatibility. (A) Bar plot representing cell cytotoxicity for HBF, MDA-MB-231, and ECs, cultured in contact with the dECM and assessed using the LDH assay. (B) Bar plot depicting the cell viability of each cell type embedded in the dECM bioink after 5 days in culture. (C) Representative maximum intensity projection (MIP) images of HBF, MDA-MB-231, and ECs (labeled in pink, green, and cyan, respectively) in the 3D dECM bioink at days 1 and 7 in culture.

viability, cells were embedded in the dECM bioink and subsequently incubated at 37 °C to allow dECM gelation. After 7 days in culture, the samples were stained with live/dead fluorophores to determine the proportion of each population, indicating that cell viability was above 80% (Fig. 2B and S5). Additionally, by staining cells with CellTracker fluorophores prior to embedding in the bioink, cell proliferation and distribution could be studied over time. Cells were homogeneously distributed in the gels and demonstrated increased proliferation and expansion over time within the dECM 3D culture, thereby confirming the biocompatible nature of this material (Fig. 2C, Fig. S6A). For completion, we examined the behavior of cells inside the dECM bioink. Cells embedded in dECM bioink featured cellular filopodia extending towards the surrounding matrix, a clear sign of cell-dECM interactions, which is crucial to correctly mimic the TME (Fig. 6B). Overall, our data suggest that the dECM bioink formulation provides a natural scaffold for cells to adhere and proliferate, thereby enabling a more accurate replication of the cell-matrix interactions found *in vivo* and offering a physiologically relevant, complex platform for recreating the behavior of

tumor cells.

3.3. Bioprinted 3D breast tumor constructs

We have shown so far that our dECM bioink has suitable rheological properties for extrusion printing, in addition to providing a suitable setting for cell growth and expansion. However, while attempting to print the dECM into a 3D construct, the formulation showed poor shape fidelity, i.e., it failed to retain the shape of the printed construct. We thus explored the addition of various rheological modifiers to improve the viscosity of the ink, such as methacrylated hyaluronic acid (HAMA), because HA is known to be overexpressed in breast tumors [52], while being biocompatible with mammalian cells. The incorporation of HAMA into the dECM bioink formulation resulted in an increase of viscosity and improved printability, compared to the pure dECM (Fig. 3A and S7), in addition to allowing a method to rapidly cross-link the dECM material under UV light irradiation. Rheological characterization of the cross-linked dECM/HAMA bioink showed a higher storage modulus than

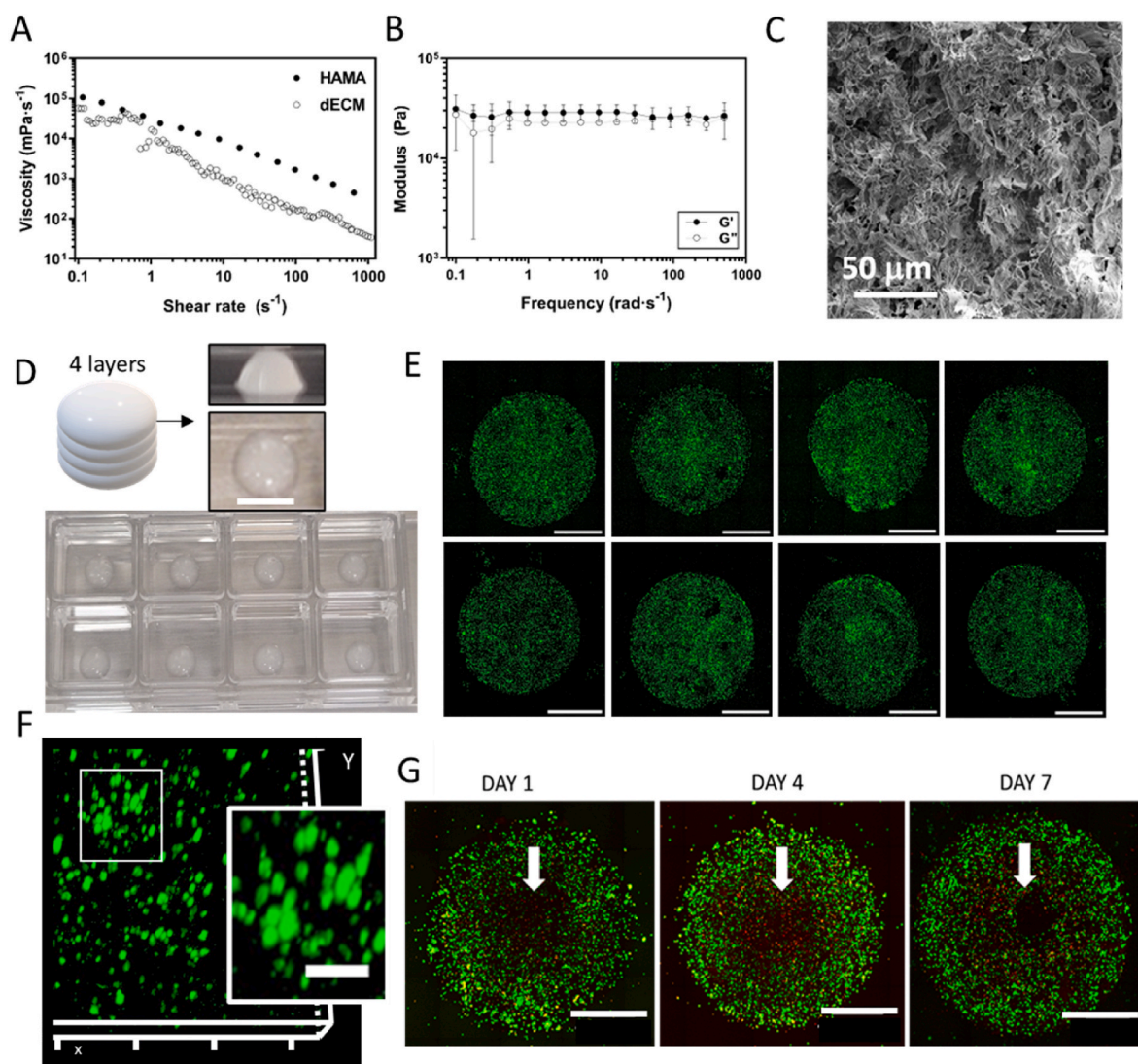


Fig. 3. Development of TNBC 3D bioprinted tumor. (A) Flow curves for non-cross-linked dECM and for a dECM/HAMA bioink. (B) Frequency sweep for cross-linked dECM/HAMA gels at 37 °C. (C) Representative SEM image of a dECM/HAMA cross-linked gel. (D) Diagram and photographs showing the 4-layered printing design and replicates of 3D-bioprinted and cross-linked tumor core structures inside 1 cm² wells. Scale bar: 2.5 mm. (E) Confocal live MIP fluorescence images of 3D bioprinted tumor core structures, showing green CellTracker labeled MDA-MB-231 cells distributed within the 3D structure. Scale bars: 1 mm. (F) 3D image reconstruction of MDA-MB-231 cells growing in a dECM/HAMA bioink. Axis marks: 200 μm. Inset scale bar: 100 μm. (G) Confocal MIP fluorescence images of 3D-bioprinted tumor model viability, at days 1, 4, and 7 in culture, assessed by live/dead (green/red) assay staining. White arrows indicate the formation of the necrotic core. Scale bars: 1 mm.

the one obtained after cross-linking the pure dECM. According to the reported storage modulus values for healthy breast tissue, the higher values recorded for the cross-linked dECM/HAMA bioink rendered it suitable to reproduce stiffer tumoral tissue. SEM images of the cross-linked dECM/HAMA mixture showed a homogeneous porous matrix, providing a suitable environment for 3D cell growth (Fig. 3C and S8A,B). Indeed, viability tests showed that dECM/HAMA was biocompatible for MDA-MB-231 cells (Fig. S8C).

To produce the 3D tumor model, MDA-MB-231 tumor cells suspended in dECM/HAMA bioink were printed by extrusion printing in the center of a 1 cm² well (Ibidi 8-well imaging slides) and exposed to UV light for cross-linking. The printing design consisted of a 4-layered circle structure with a diameter of 1 mm. Detailed information on the tumor core bioprinting design and dimensions is shown in Fig. S9A. Live fluorescence microscopy showed MDA-MB-231 cells homogeneously

distributed within the bioink. Additionally, bioprinted replicates showed high similarity in size, shape and morphology, indicating the efficiency of the bioprinting technology to render reproducible structures (Fig. 3D and E). MDA-MB-231 cells were observed, both as single cells and forming 3D aggregates (Fig. 3F). Again, we used live/dead fluorophore staining to determine the viability of MDA-MB-231 cells, 1, 4, and 7 days post printing. A necrotic core containing dead cells (red, positive for propidium iodide) was identified at the center of the tumor constructs, whereas the cells found in the outer ca. 1 mm area were alive (green, positive for Calcein) (Fig. 3G). This necrotic core might be attributed to different parameters such as low oxygen and nutrient supply to the cancer cells remaining in the inner part of the tumor [53].

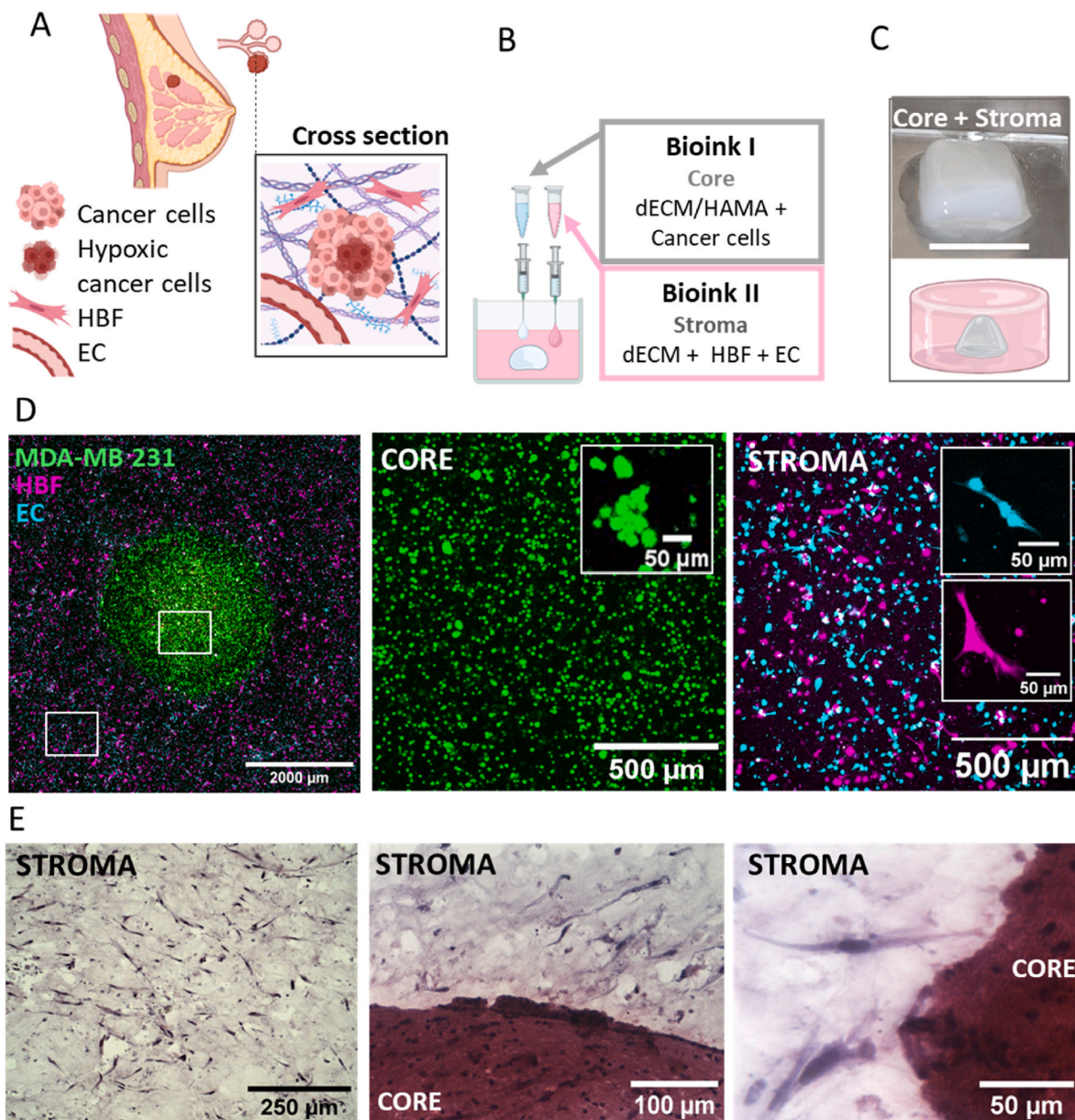


Fig. 4. 3D-bioprinted breast TNBC tumor-stroma model. (A) Schematic illustration of the main components of a breast tumor niche. (B) Diagram illustrating the preparation of a bioprinted tumor-stroma construct. (C) Representative examples of bioprinted and cross-linked tumor (top) and tumor-stroma (bottom) models. Scale bars: 2 mm (core) and 1 cm (stroma). A diagram of the entire model is also depicted. (D) Live-cell confocal MIP fluorescence images depicting an inner core composed of MDA-MB-231 breast tumor cells (green), surrounded by HBF (pink) and EC (cyan) stromal cells. (E) Representative H&E images of 3D printed tumor tissue sections after 7 days in culture. Images show both the stromal and tumor core compartments.

3.4. Bioprinted 3D tumor-stroma models recapitulate cellular components and tissue architecture of breast TME

The tumor stroma, whose functions are orchestrated by precise spatial organization of specialized cells, plays a pivotal role in tumorigenesis, metastatic spread, and response to therapies [10,11]. Aiming at faithfully recreating the complexity of breast TME, we developed a bioprinted TNBC tumor-stroma 3D model encompassing both tumor and stromal cell types, within pre-defined architectures. The design of the model was inspired by the spatial arrangement of breast carcinomas, comprising a central core made of tumor cells, surrounded by a stromal cell compartment, closely mirroring the breast tumor niche (Fig. 4A) [54]. For the desired architecture of the model to be created, we employed two different bioinks (Fig. 4B). Bioink 1, made of dECM/HAMA, was selected to create the tumor core because of its better printability, required to maintain the shape of the tumor prior to adding the stromal compartment. Bioink 2, comprising the unmodified dECM, was used to recreate the stromal compartment, which did not require as much shape fidelity to surround the cancer core. The 3D TNBC tumor-stroma model was thus produced by first printing the MDA-MB-231 tumor cells core embedded in the Bioink1 and cross-linking with UV light, followed by addition of HBF and EC stromal cells mixed with Bioink 2 to envelop the cancer core (Fig. 4B). Specifications of the printing design and constructs architecture are detailed in Materials and Methods section and in Fig. S9A. The bioprinted models were then incubated at 37 °C to promote dECM bioink cross-linking. When necessary, cells were pre-labeled with CellTracker probes to study their morphology and proliferation in live cultures. The printed models, with approximate dimensions of 1 cm × 1 cm × 5 mm, could be reproduced in a variety of cell culture slides and plates. Representative photographs of the cancer core (after UV cross-linking) and tumor-stroma models (after temperature cross-linking) are presented in Fig. 4C. Confocal MIP fluorescence images of various replicates of the final model and magnifications of both compartments revealed the native cellular morphology, suggestive of an optimum ECM environment for each cell type (Fig. 4D and Figs. S9 and S10). More specifically, tumor cells within the core grew into aggregates mirroring typically observed tumor 3D growth, whereas HBFs and ECs displayed elongated fibroblast and endothelial cell morphologies, respectively. Viability tests at day 7 in culture revealed that the majority of cells remained viable, with the exception of the necrotic core (Fig. S11). These observations were confirmed using histological staining techniques, which revealed high cell densities in all three dimensions and the expected cell morphologies (Fig. 4E and Fig. S12). Altogether, these findings highlight the ability of our 3D-bioprinted *in vitro* model to recapitulate important pivotal aspects of the breast TME.

3.5. 3D tumor-stroma models recapitulate the biological activity of the TNBC TME

Reciprocal reprogramming of tumor cells and the surrounding stromal cells towards a tumor-promoting state drives cancer progression [11,55,56]. Therefore, we sought to study whether our model could mirror the activation of a tumor promoting TME, which required more in-depth functional and biological characterization. 3D tumor-stroma models were cultured for 7 days and evaluated by immunofluorescence (IF). IF staining confirmed that MDA-MB-231 cells within the tumor core expressed SLUG and TWIST-1 biomarkers, whereas no signal for these markers was detected in the stromal compartment (Fig. 5A). Since multiple studies have shown that SLUG and TWIST-1 factors play important roles in promoting the EMT process, tumor progression and metastasis in TNBC cells [57,58], we conclude that our model does reflect the aggressive nature of TNBC tumors. Indeed, the expression of these factors is usually associated with CSCs within tumors, which are particularly overrepresented in TNBC [59]. Immunofluorescence imaging revealed that certain tumor cells exhibited co-staining for the

stemness markers OCT-4, NANOG, and ALDH1A1, as would be expected for the formation of CSC-like populations in the model (Fig. S13). Additionally, we detected high levels of TGF- β 1 in both the tumor and the stromal compartments. The TGF- β 1 signaling pathway plays a crucial role in the communication between breast cancer cells and cancer-associated fibroblasts (CAFs), because it can activate the expression of EMT-related factors [60–62]. The TGF- β 1 expression pattern suggested the development of an active paracrine signaling loop between cancer cells and CAFs, where TGF- β 1 produced by CAFs would stimulate tumor cell growth through EMT induction. We additionally evaluated the expression of vimentin, an intermediate filament protein that is commonly used as a marker of increased malignancy in breast tumors [63]. Vimentin was found to be widely expressed in the tumor core compartment, which is consistent with the presence of tumor cells presenting EMT phenotype in TNBC cells [64–66]. Additionally, extensive expression of vimentin and α -smooth muscle actin (α -SMA) biomarkers of CAF activation [63,67], was identified in the stromal compartment (Fig. 5B). Detailed image analysis of the stroma showed fibroblast-like populations with double staining for vimentin and α -SMA biomarkers, indicating the formation of CAFs in the 3D model (Fig. 5C, Fig. S14). CAFs play crucial roles in tumor progression because they are key mediators of processes such as tumor growth, invasion, angiogenesis, and immunosuppression. Indeed, the increased expression of α -SMA and vimentin in the TME has been correlated with poor prognosis in breast cancer [63]. To study the presence of ECs, we next analyzed the expression pattern of CD31, an adhesion molecule involved in cell-cell interaction for endothelial cells, which also plays an important role in neovascularization [68]. CD31 was expressed in both control 2D cultures and in the 3D stroma model, showing EC clustering, suggestive of angiogenic processes (Fig. 5D).

To characterize the functionality of the model, cell culture media supernatants were collected from four different conditions: acellular dECM, stroma alone (HBF + EC in dECM), core alone (MDA-MB-231 in dECM/HAMA), and the complete 3D tumor-stroma model. The samples were analyzed using a microarray cytokine-profiler composed of 96 conjugated antibodies. Image of the membranes used for analysis are depicted in Fig. S14D. Detected cytokines were then categorized according to their effects on tumor biology, with important differences being observed for different conditions (Fig. 5E). For example, upregulation of IL-8 was clearly identified in both the tumor and tumor-stroma models, compared to the dECM (3-fold increase) and stroma (1.4-fold increase). Of note, dECM rendered no signal for any of the analyzed cytokines, except for IL-8, which plays a crucial role in the breast TME by attracting proinflammatory immune cells, promoting angiogenesis and tumor cell invasion, regulating CSC populations, and increasing resistance to therapy [69–72]. In agreement with IF analysis, we also observed an upregulation of CD31 in the tumor-stroma model, compared to stroma (2-fold increase). This enhancement likely results from the interaction between tumor cells and ECs, which triggers EC proliferation to support the tumor's nutrient supply. Extracellular Matrix Protein-1 (EMPRIN), closely linked to breast tumor invasion [73, 74], was upregulated by 1.2 and 14.7 times in the tumor-stroma model, compared to stroma and tumor core models, respectively, indicating the importance of the 3D stroma in the secretion of cytokines involved in ECM remodeling. Finally, macrophage migration inhibitory factor (MIF), granulocyte-macrophage colony-stimulating factor (GM-CSF), and PENTRAXIN, all cytokines that promote breast tumor growth through immune cell proliferation and activation [75,76], were upregulated in the 3D tumor-stroma model, reproducing the inflammatory nature of the TNBC TME.

We therefore conclude that the model effectively recapitulates key features of TNBC tumors biology and replicates the biological activity and molecular pathways typically observed in the activated TME.

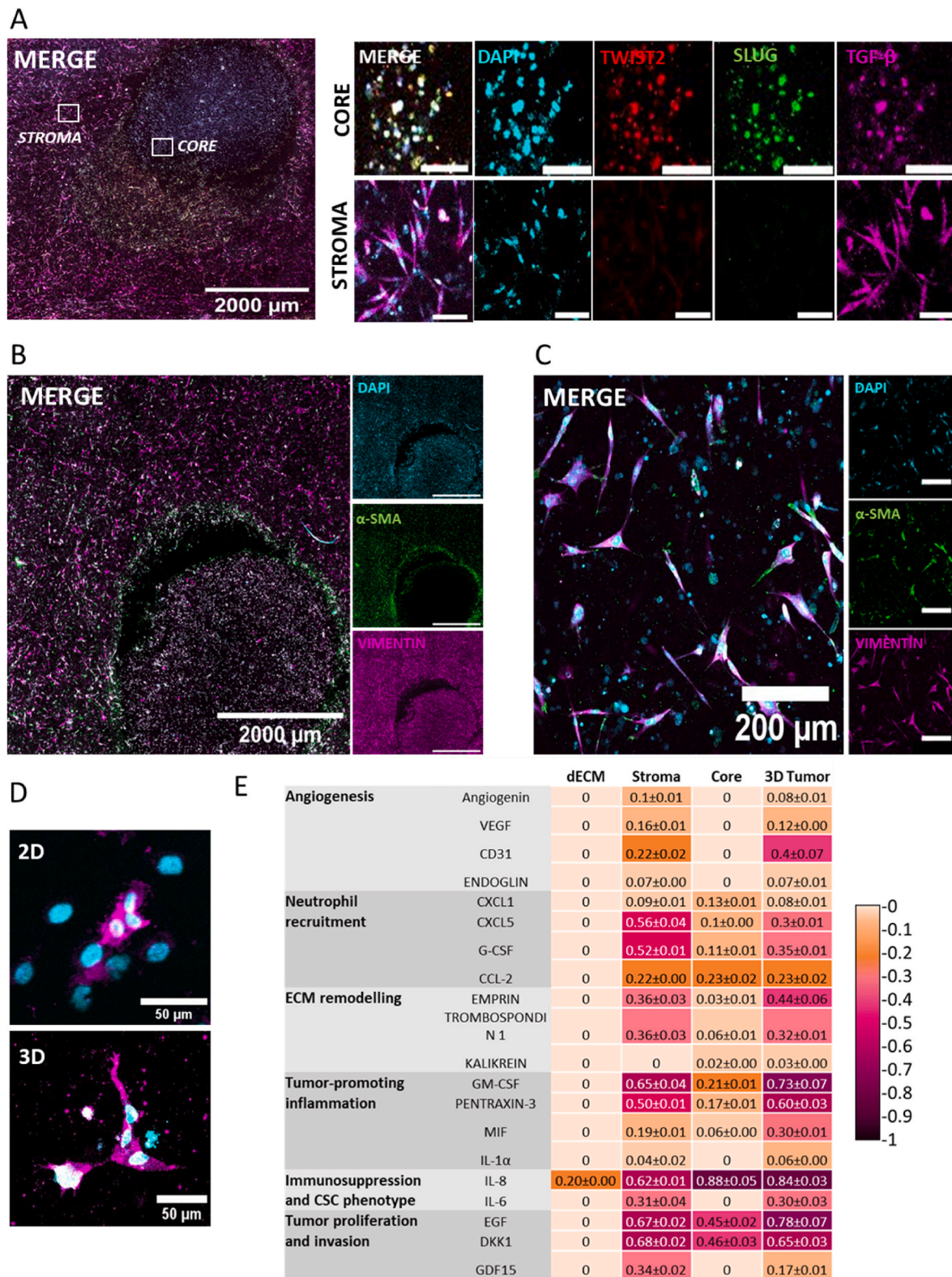


Fig. 5. Biological characterization of biprinted breast MDA-MB-231 tumor-stroma model. (A) Representative IF images of the 3D model stained for TWIST 2 (red), SLUG (green), and TGF-B (pink), for the analysis of EMT progression in tumor cells, and with DAPI (cyan) for cell nuclei. Magnifications of both the core (top) and stromal (bottom) compartments are included. Scale bars in the insets: 100 μm. (B) Representative IF images of the 3D model stained for α-SMA (green), vimentin (pink), and DAPI (cyan). Scale bars: 2000 μm. (C) Representative magnified image of the stromal compartment, stained for α-SMA (green) and vimentin (pink) to identify CAF populations, and with DAPI (cyan) for cell nuclei. Scale bars: 200 μm. (D) Representative IF images against CD31 (pink) for EC identification in 2D culture (top) and in the 3D stromal compartment (bottom). Scale bars: 50 μm. (E) Heat-map indicating the cytokine secretion pattern in dECM, stroma, core, and tumor-stroma 3D models, measured using a microarray cytokine profiler. Integrated density values are represented as Mean ± Standard deviation.

3.6. Bioprinted tumor models to assess therapeutic efficacy

The TME is an essential factor for adequate evaluation of the response of cancer cells against drugs [77]. Therefore, it is crucial to maintain the natural TME characteristics when designing *in vitro* tumor models for pre-clinical drug testing. Aiming to establish a drug testing platform, we employed various 3D tumor-stroma models representing distinct clinical tumor subtypes (Fig. 6A). We therefore developed a new hormone-dependent 3D breast tumor model containing MCF-7 cells, as opposed to MDA-MB-231 cells, in the tumor core compartment. A representative multilabeled fluorescence image of the MCF-7 tumor-stroma model is depicted in Fig. S15. Both MDA-MB-231 and MCF-7 3D-tumor-stroma models were bioprinted in 48-well microplates to simultaneously test their sensitivity to different drug compounds. Bioprinting allowed us to automatically and sequentially print a large number of 3D tumor-stroma models, resulting in a high-throughput drug testing platform (Fig. 6B). After 1 day in culture, 3D models were exposed to increasing concentrations of Doxorubicin and Paclitaxel, two prominent chemotherapeutic compounds in breast cancer. After 72 h of

treatment, cytotoxicity tests were applied to study drug efficacy in each 3D tumor-stroma model subtype. The results showed that Paclitaxel and Doxorubicin showed cytotoxic effects in both MDA-MB-231 and MCF-7 bioprinted tissue models (Fig. 6C and D). However, whereas MCF-7 models showed a positive correlation between drug concentration and cell cytotoxicity, MDA-MB-231 models did not show any clear trend in response to varying drug concentrations. This result could be explained by the molecular heterogeneity of the MDA-MB-231 cell line, because TNBC is known to present different subclones with different drug resistance profiles within the same tumor [78]. Finally, we tested the use of targeted therapies in our bioprinted model, with the example of Tamoxifen, a selective estrogen receptor (ER) modulator that inhibits growth and promotes apoptosis in ER + tumors. Whereas MDA-MB-231 cells lack ER, MCF-7 cells express the ER and thus depend on estrogen to proliferate. As shown in Fig. 6E, MCF-7 tumor-stroma models were Tamoxifen dose-dependent, with a clear cytotoxic response to increasing drug concentration. On the contrary, MDA-MB-231 3D tumor-stroma models did not show a dose-dependent cytotoxicity, maintaining values around 25% regardless of the drug concentration. Indeed,

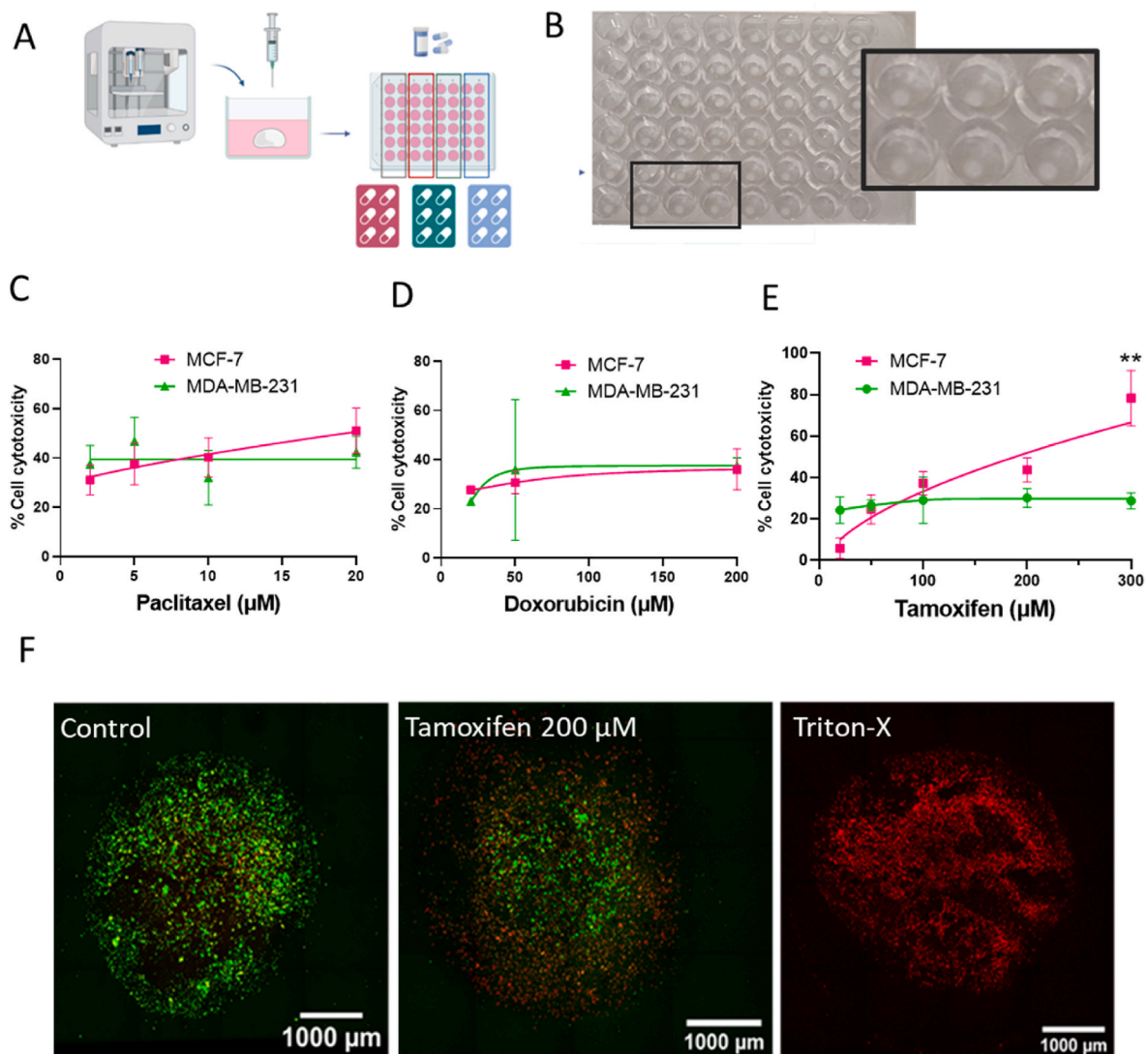


Fig. 6. Bioprinted 3D tumor-stroma models as a drug screening platform. (A) Schematic design of the development of a high-throughput drug testing platform based on 3D-bioprinted tumor-stroma models. (B) Representative photograph showing 3D-bioprinted tumor models in a high throughput 48-well plate, prior to the addition of stromal cell compartment. (C–E) Graphs depicting the drug dose-response curves in terms of cell toxicity (%) in MDA-MB-231 and MCF-7 3D tumor-stroma models, exposed for 72 h to increasing concentrations of Paclitaxel (C), Doxorubicin (D), and Tamoxifen (E). (F) Representative live confocal fluorescence images of live/dead viability tests on MCF-7 tumor models exposed to Tamoxifen (200 μM) for 72 h.

MDA-MB-231 models were significantly ($p = 0.006$) more resistant to Tamoxifen at the highest drug concentration (300 μM) than the MCF-7 3D models. As such, we verified that ER + breast tumor models (MCF-7) are more susceptible to the toxic effects of Tamoxifen, compared to ER-breast tumor models (MDA-MB-231). We additionally visualized this cytotoxicity trend by using live/dead staining of the MCF-7 3D model exposed to Tamoxifen, at a concentration equivalent to its IC_{50} (i.e., 200 μM). As shown in Fig. 6F, rather than the typical necrotic core, higher Propidium Iodide staining was seen at the outer edge of the core, suggestive of a significant drug gradient, which may hinder successful chemotherapeutic treatment of compact tumors. In summary, our findings confirm the ability of different 3D models to be used as a drug screening platform to predict the effectiveness of a given therapy. This approach could be used for the efficient screening of many compounds in a short period of time, leading to faster and more cost-effective drug discovery.

4. Conclusions

This study presents a 3D breast tumor-stroma *in vitro* model based on bioinks derived from porcine breast tissue, to imitate the structure and key features of the natural breast TME. The model captures essential characteristics, such as the complexity of the TME structure, the mechanical and biological properties of the ECM, and the heterogeneous nature of the cell populations and tumor-promoting pathways. Indeed, preclinical application of this model has been demonstrated toward screening targeted therapies for different tumor subtypes. However, to overcome the models limitations and increase the clinical significance of our bioprinted 3D model, further advancements are imperative. By incorporating extensive biomolecular characterization, immune cells, and patient-derived tumor samples into the model, we can generate a more accurate representation of the TME, its interactions with the immune system, and individual patient responses to treatment. Ultimately, this enhanced bioprinted model could have the potential to accelerate drug discovery, optimize treatment strategies, and improve patient outcomes in the field of cancer research and clinical practice.

Credit author statement

Patricia González-Callejo: Conceptualization, Methodology, Data curation, Writing – original draft, Paula Vázquez-Aristizabal: Methodology, Data curation, Writing – original draft, Clara García-Astrain: Methodology, Data curation, Writing – original draft, Dorleta Jimenez de Aberasturi: Methodology, Writing – review & editing, Malou Henriksen-Lacey: Methodology, Validation, Writing – review & editing, Ander Izeta: Conceptualization, Methodology, Resources, Writing – review & editing, Luis M. Liz-Marzán: Conceptualization, Validation, Resources, Project administration, Funding acquisition, Writing – review & editing

Declaration of competing interest

The authors declare that they have no known competing financial interests or personal relationships that could have appeared to influence the work reported in this paper.

Data availability

Data will be made available on request.

Acknowledgements

Financial support is acknowledged from the European Research Council (ERC Advanced Grant 787510, 4DbioSERS) and MCIN/AEI /10.13039/501100011033 through project # PID2019-108854RA-I00. C.G.A acknowledges a Juan de la Cierva Incorporación fellowship

(IJC2019-040827-I). P.V.A. and A.I. thank Katxalin Asociación de Mujeres Afectadas de Cáncer de Mama y Ginecológico de Guipúzcoa for their donation and Project PI22/01247, funded by Instituto de Salud Carlos III (ISCIII) and co-funded by the European Union.

Received: ((will be filled in by the editorial staff)) Revised: ((will be filled in by the editorial staff)) Published online: ((will be filled in by the editorial staff))

Appendix A. Supplementary data

Supplementary data to this article can be found online at <https://doi.org/10.1016/j.mtbio.2023.100826>.

Supporting Information

Supporting Information is available from the Wiley Online Library or from the author.

References

- [1] H. Sung, J. Ferlay, R.L. Siegel, M. Laversanne, I. Soerjomataram, A. Jemal, F. Bray, Global cancer statistics 2020: GLOBOCAN estimates of incidence and mortality worldwide for 36 cancers in 185 countries, *CA Cancer J Clin* 71 (2021) 209–249, <https://doi.org/10.3322/caac.21660>.
- [2] S. Koren, M. Bentires-Alj, Breast tumor heterogeneity: source of fitness, hurdle for therapy, *Mol Cell* 60 (2015) 537–546, <https://doi.org/10.1016/j.molcel.2015.10.031>.
- [3] R. Dent, M. Trudeau, K.I. Pritchard, W.M. Hanna, H.K. Kahn, C.A. Sawka, L. A. Lickley, E. Rawlinson, P. Sun, S.A. Narod, Triple-negative breast cancer: clinical features and patterns of recurrence, *Clin. Cancer Res.* 13 (2007) 4429–4434, <https://doi.org/10.1158/1078-0432.CCR-06-3045>.
- [4] B.D. Lehmann, J.A. Bauer, X. Chen, M.E. Sanders, A.B. Chakravarthy, Y. Shyr, J. A. Pietenpol, Identification of human triple-negative breast cancer subtypes and preclinical models for selection of targeted therapies, *J. Clin. Invest.* 121 (2011) 2750–2767, <https://doi.org/10.1172/JCI45014>.
- [5] C. Pauli, B.D. Hopkins, D. Prandi, R. Shaw, T. Fedrizzi, A. Sboner, V. Sailer, M. Augello, L. Puca, R. Rosati, T.J. McNary, Y. Churakova, C. Cheung, J. Triscott, D. Pisapia, R. Rao, J.M. Mosquera, B. Robinson, B.M. Faltas, B.E. Emerling, V. K. Gadi, B. Bernard, O. Elemento, H. Beltran, F. Demicheli, C.J. Kemp, C. Grandori, L.C. Cantley, M.A. Rubin, Personalized *in vitro* and *in vivo* cancer models to guide precision medicine, *Cancer Discov.* 7 (2017) 462–477, <https://doi.org/10.1158/2159-8290.CD-16-1154>.
- [6] R. Bartlett, W. Everett, S. Lim, G. Natasha, M. Loizidou, G. Jell, A. Tan, A. M. Seifalian, Personalized *in vitro* cancer modeling — fantasy or reality? *Transl Oncol* 7 (2014) 657–664, <https://doi.org/10.1016/j.tranon.2014.10.006>.
- [7] V. Veninga, E.E. Voest, Tumor organoids: opportunities and challenges to guide precision medicine, *Cancer Cell* 39 (2021) 1190–1201, <https://doi.org/10.1016/j.ccell.2021.07.020>.
- [8] B.L. LeSavage, R.A. Suhar, N. Broguiere, M.P. Lutolf, S.C. Heilshorn, Next-generation cancer organoids, *Nat. Mater.* 21 (2022) 143–159, <https://doi.org/10.1038/s41563-021-01057-5>.
- [9] W. Asghar, R. El Assal, H. Shafiee, S. Pitteri, R. Paulmurugan, U. Demirci, Engineering cancer microenvironments for *in vitro* 3-D tumor models, *Mater. Today* 18 (2015) 539–553, <https://doi.org/10.1016/j.mattod.2015.05.002>.
- [10] N.M. Anderson, M.C. Simon, The tumor microenvironment, *Curr. Biol.* 30 (2020) R921, <https://doi.org/10.1016/j.cub.2020.06.081>. –R925.
- [11] T.L. Whiteside, The tumor microenvironment and its role in promoting tumor growth, *Oncogene* 27 (2008) 5904–5912, <https://doi.org/10.1038/onc.2008.271>.
- [12] S. V Murphy, A. Atala, 3D bioprinting of tissues and organs 32 (2014) 773–785, <https://doi.org/10.1038/nbt.2958>.
- [13] P. Datta, M. Dey, Z. Ataie, D. Unutmaz, I.T. Ozbolat, 3D bioprinting for reconstituting the cancer microenvironment, *npj Precis. Oncol.* 4 (2020) 18, <https://doi.org/10.1038/s41698-020-0121-2>.
- [14] Y.S. Zhang, M. Duchamp, R. Oklu, L.W. Ellisen, R. Langer, A. Khademhosseini, Bioprinting the cancer microenvironment, *ACS Biomater. Sci. Eng.* 2 (2016) 1710–1721, <https://doi.org/10.1021/acsbiomaterials.6b00246>.
- [15] N. Germain, M. Dhayer, S. Dekiok, P. Marchetti, Current advances in 3D bioprinting for cancer modeling and personalized medicine, *Int. J. Mol. Sci.* 23 (2022) 3432, <https://doi.org/10.3390/ijms23073432>.
- [16] R. Augustine, S.N. Kalva, R. Ahmad, A.A. Zahid, S. Hasan, A. Nayeem, L. McClements, A. Hasan, 3D Bioprinted cancer models: revolutionizing personalized cancer therapy, *Transl Oncol* 14 (2021), 101015, <https://doi.org/10.1016/j.tranon.2021.101015>.
- [17] S. Mao, Y. Pang, T. Liu, Y. Shao, J. He, H. Yang, Y. Mao, W. Sun, Bioprinting of *in vitro* tumor models for personalized cancer treatment: a review, *Biofabrication* 12 (2020), 042001, <https://doi.org/10.1088/1758-5090/ab97c0>.
- [18] F.L.C. Morgan, L. Moroni, M.B. Baker, Dynamic bioinks to advance bioprinting, *Adv. Healthcare Mater.* 9 (2020), 1901798, <https://doi.org/10.1002/adhm.201901798>.

- [19] N. Ashammakhi, S. Ahadian, C. Xu, H. Montazerian, H. Ko, R. Nasiri, N. Barros, A. Khademhosseini, Bioinks and bioprinting technologies to make heterogeneous and biomimetic tissue constructs, *Mater Today Bio* 1 (2019), 100008, <https://doi.org/10.1016/j.mtbio.2019.100008>.
- [20] Y. Gu, A. Forget, V.P. Shastri, Biobridge: an outlook on translational bioinks for 3D bioprinting, *Adv. Sci.* 9 (2022), 2103469, <https://doi.org/10.1002/adv.202103469>.
- [21] R. Khoehi, H. Nosrati, A. Akbarzadeh, A. Eftekhari, T. Kavetskiy, R. Khalilov, E. Ahmadian, A. Nasibova, P. Datta, L. Roshangar, D.C. Deluca, S. Davaran, M. Cucchiari, I.T. Ozbolat, Natural and synthetic bioinks for 3D bioprinting, *Adv Nanobiomed Res* 1 (2021), 2000097, <https://doi.org/10.1002/anbr.202000097>.
- [22] A. Abaci, M. Guvendiren, Designing decellularized extracellular matrix-based bioinks for 3D bioprinting, *Adv. Healthcare Mater.* 9 (2020), 2000734, <https://doi.org/10.1002/adhm.202000734>.
- [23] L.P. Ferreira, V.M. Gaspar, J.F. Mano, Decellularized extracellular matrix for bioengineering physiologic 3D in vitro tumor models, *Trends Biotechnol.* 38 (2020) 1397–1414, <https://doi.org/10.1016/j.tibtech.2020.04.006>.
- [24] F. Meng, C.M. Meyer, D. Joung, D.A. Vallera, M.C. McAlpine, A. Panoskaltis-Mortari, 3D bioprinted in vitro metastatic models via reconstruction of tumor microenvironments, *Adv. Mater.* 31 (2019), 1806899, <https://doi.org/10.1002/adma.201806899>.
- [25] E.M. Langer, B.L. Allen-Petersen, S.M. King, N.D. Kendsersky, M.A. Turnidge, G. M. Kuziel, R. Riggers, R. Samatham, T.S. Amery, S.L. Jacques, B.C. Sheppard, J. E. Korkola, J.L. Muschler, G. Thibault, Y.H. Chang, J.W. Gray, S.C. Presnell, D. G. Nguyen, R.C. Sears, Modeling tumor phenotypes in vitro with three-dimensional bioprinting, *Cell Rep.* 26 (2019) 608–623, <https://doi.org/10.1016/j.celrep.2018.12.090>. E6.
- [26] H.G. Yi, Y.H. Jeong, Y. Kim, Y.J. Choi, H.E. Moon, S.H. Park, K.S. Kang, M. Bae, J. Jang, H. Youn, S.H. Paek, D.W. Cho, A bioprinted human-glioblastoma-on-a-chip for the identification of patient-specific responses to chemoradiotherapy, *Nat. Biomed. Eng.* 3 (2019) 509–519, <https://doi.org/10.1038/s41551-019-0363-x>.
- [27] L. Neufeld, E. Yeini, N. Reisman, Y. Shitlerman, D. Ben-Shushan, S. Pozzi, A. Madi, G. Tiram, A. Eldar-Boock, S. Ferber, R. Grossman, Z. Ram, R. Satchi-Fainaro, Microengineered perfusable 3D-bioprinted glioblastoma model for in vivo mimicry of tumor microenvironment, *Sci. Adv.* 7 (2022), <https://doi.org/10.1126/sciadv.abi9119>.
- [28] Y. Chen, L. Xu, W. Li, W. Chen, Q. He, X. Zhang, J. Tang, Y. Wang, B. Liu, J. Liu, 3D bioprinted tumor model with extracellular matrix enhanced bioinks for nanoparticle evaluation, *Biofabrication* 14 (2022), 025002, <https://doi.org/10.1088/1758-5090/ac48e4>.
- [29] P.A. Mollica, E.N. Booth-Creech, J.A. Reid, M. Zamponi, S.M. Sullivan, X.L. Palmer, P.C. Sachs, R.D. Bruno, 3D bioprinted mammary organoids and tumours in human mammary derived ECM hydrogels, *Acta Biomater.* 95 (2019) 201–213, <https://doi.org/10.1016/j.actbio.2019.06.017>.
- [30] M.R. Green, J. Sambrook, Precipitation of DNA with ethanol, *Cold Spring Harb. Protoc.* 2016 (2016) 1116–1120, <https://doi.org/10.1101/pdb.prot093377>.
- [31] J.R. Wisniewski, A. Zougman, N. Nagaraj, M. Mann, Universal sample preparation method for proteome analysis, *Nat. Methods* 6 (2009) 359–362, <https://doi.org/10.1038/nmeth.1322>.
- [32] J. Cox, M. Mann, MaxQuant enables high peptide identification rates, individualized p.p.b.-range mass accuracies and proteome-wide protein quantification, *Nat. Biotechnol.* 26 (2008) 1367–1372, <https://doi.org/10.1038/nbt.1511>.
- [33] R.O. Hynes, A. Naba, Overview of the matrisome—An inventory of extracellular matrix constituents and functions, *Cold Spring Harbor Perspect. Biol.* 4 (2012) 1–16, <https://doi.org/10.1101/cshperspect.a004903>.
- [34] B. Blanco-Fernandez, S. Rey-Vinolas, G. Baççal, G. Rubi-Sans, J. Otero, D. Navajas, S. Perez-Amodio, E. Engel, Bioprinting decellularized breast tissue for the development of three-dimensional breast cancer models, *ACS Appl. Mater. Interfaces* 14 (2022), 29467, <https://doi.org/10.1021/acsami.2c00920>. –29482.
- [35] P.M. Crapo, T.W. Gilbert, S.F. Badylak, An overview of tissue and whole organ decellularization processes, *Biomaterials* 32 (2011) 3233–3243, <https://doi.org/10.1016/j.biomaterials.2011.01.057>.
- [36] T. Umamoto, E. Ueno, T. Matsumura, M. Yamakawa, H. Bando, T. Mitake, T. Shiina, Ex vivo and in vivo assessment of the non-linearity of elasticity properties of breast tissues for quantitative strain elastography, *Ultrasound Med. Biol.* 40 (2014) 1755–1768, <https://doi.org/10.1016/j.ultrasmedbio.2014.02.005>.
- [37] Z. Xie, A. Bailey, M.V. Kuleshov, D.J.B. Clarke, J.E. Evangelista, S.L. Jenkins, A. Lachmann, M.L. Wojciechowicz, E. Kropiwnicki, K.M. Jagodnik, M. Jeon, A. Ma'ayan, Gene set knowledge discovery with enrichr, *Curr Protoc* 1 (2021) 1–51, <https://doi.org/10.1002/cpz1.90>.
- [38] H. Lin, B. Chen, W. Sun, W. Zhao, Y. Zhao, J. Dai, The effect of collagen-targeting platelet-derived growth factor on cellularization and vascularization of collagen scaffolds, *Biomaterials* 27 (2006) 5708–5714, <https://doi.org/10.1016/j.biomaterials.2006.07.023>.
- [39] P. Juhl, S. Bondesen, C.L. Hawkins, M.A. Karsdal, A.C. Bay-Jensen, M.J. Davies, A. S. Siebühr, Dermal fibroblasts have different extracellular matrix profiles induced by TGF- β , PDGF and IL-6 in a model for skin fibrosis, *Sci. Rep.* 10 (2020) 1–10, <https://doi.org/10.1038/s41598-020-74179-6>.
- [40] J.H. Sun, M. Huang, Z. Fang, T.X. Li, T.T. Wu, Y. Chen, D.P. Quan, Y.Y. Xu, Y. M. Wang, Y. Yang, J.L. Zou, Nerve bundle formation during the promotion of peripheral nerve regeneration: collagen VI-neural cell adhesion molecule 1 interaction, *Neural Regen Res* 17 (2022) 1023–1033, <https://doi.org/10.4103/1673-5374.324861>.
- [41] C. Denis, D. Baruch, C.M. Kieley, N. Ajzenberg, O. Christophe, D. Meyer, Localization of von Willebrand factor binding domains to endothelial extracellular matrix and to type VI collagen, *Arterioscler. Thromb.* 13 (1993) 398–406, <https://doi.org/10.1161/01.atv.13.3.398>.
- [42] B. Alberts, A. Johnson, J. Lewis, M. Raff, K. Roberts, P. Walter, *Molecular biology of the cell*, in: *Mol Biol Cell*, fifth ed., Garland Science, New York, 2008, pp. 1131–1204.
- [43] D. Lau, H. Wadhwa, S. Sudhir, A.C.C. Chang, S. Jain, A. Chandra, A.T. Nguyen, J. M. Spatz, A. Pappu, S.S. Shah, J. Cheng, M.M. Safaei, G. Yagnik, A. Jahangiri, M. K. Aghi, Role of c-met/ β 1 integrin complex in the metastatic cascade in breast cancer, *JCI Insight* 6 (2021) 1–14, <https://doi.org/10.1172/jci.insight.138928>.
- [44] Y. Takada, Y.K. Takada, M. Fujita, Crosstalk between insulin-like growth factor (IGF) receptor and integrins through direct integrin binding to IGF1, *Cytokine Growth Factor Rev.* 34 (2017) 67–72, <https://doi.org/10.1016/j.cytogfr.2017.01.003>.
- [45] S.S. Skandalis, N. Afratis, G. Smirlaki, D. Nikitovic, A.D. Theocharis, G. N. Tzanakakis, N.K. Karamanos, Cross-talk between estradiol receptor and EGFR/IGF-IR signaling pathways in estrogen-responsive breast cancers: focus on the role and impact of proteoglycans, *Matrix Biol.* 35 (2014) 182–193, <https://doi.org/10.1016/j.mtbio.2013.09.002>.
- [46] J.L. Martin, S. Jambazov, Insulin-like growth factor binding protein-3 in extracellular matrix stimulates adhesion of breast epithelial cells and activation of p44/42 mitogen-activated protein kinase, *Endocrinology* 147 (2006) 4400–4409, <https://doi.org/10.1210/en.2006-0094>.
- [47] R. Butti, S. Das, V.P. Gunasekaran, A.S. Yadav, D. Kumar, G.C. Kundu, Receptor tyrosine kinases (RTKs) in breast cancer: signaling, therapeutic implications and challenges, *Mol. Cancer* 17 (2018) 1–18, <https://doi.org/10.1186/s12943-018-0797-x>.
- [48] X. Fu, C.K. Osborne, R. Schiff, Biology and therapeutic potential of PI3K signaling in ER+/HER2-negative breast cancer, *Breast* 22 (2013), <https://doi.org/10.1016/j.breast.2013.08.001>. S12–S18.
- [49] M. Shen, Y.Z. Jiang, Y. Wei, B. Ell, X. Sheng, M. Esposito, J. Kang, X. Hang, H. Zhang, M. Rowicki, L. Zhang, W.J. Shih, T. Celià-Terrassa, Y. Liu, I. Cristea, Z. M. Shao, Y. Kang, Tinag1 suppresses triple-negative breast cancer progression and metastasis by simultaneously inhibiting integrin/FAK and EGFR signaling, *Cancer Cell* 35 (2019) 64–80, <https://doi.org/10.1016/j.ccell.2018.11.016>.
- [50] L. Zhang, J. Qu, Y. Qi, Y. Duan, Y.W. Huang, Z. Zhou, P. Li, J. Yao, B. Huang, S. Zhang, D. Yu, EZH2 engages TGF β signaling to promote breast cancer bone metastasis via integrin β 1-FAK activation, *Nat. Commun.* 13 (2022) 2543, <https://doi.org/10.1038/s41467-022-30105-0>.
- [51] M. Allinen, R. Beroukhi, L. Cai, C. Brennan, J. Lahti-Domenici, H. Huang, D. Porter, M. Hu, L. Chin, A. Richardson, S. Schmitt, W.R. Sellers, K. Polyak, Molecular characterization of the tumor microenvironment in breast cancer, *Cancer Cell* 6 (2004) 17–32, <https://doi.org/10.1016/j.ccr.2004.06.010>.
- [52] K.L. Schwertfeger, M.K. Cowman, P.G. Telmer, E.A. Turley, J.B. McCarthy, Hyaluronan, inflammation, and breast cancer progression, *Front. Immunol.* 6 (2015) 236, <https://doi.org/10.3389/fimmu.2015.00236>.
- [53] D. Jiao, Z. Cai, S. Choksi, D. Ma, M. Choe, H.J. Kwon, J.Y. Baik, B.G. Rowan, C. Liu, Z.G. Liu, Necroptosis of tumor cells leads to tumor necrosis and promotes tumor metastasis, *Cell Res.* 28 (2018) 868–870, <https://doi.org/10.1038/s41422-018-0058-y>.
- [54] J. Almagro, H.A. Messal, A. Elosegui-Artola, J. van Rheenen, A. Behrens, Tissue architecture in tumor initiation and progression, *Trends Cancer* 8 (2022), <https://doi.org/10.1016/j.trecan.2022.02.007>.
- [55] R. Burgos-Panadero, F. Lucantoni, E. Gamero-Sandemeterio, L. de la Cruz-Merino, T. Álvaro, R. Noguera, The tumour microenvironment as an integrated framework to understand cancer biology, *Cancer Lett.* 461 (2019) 112–122, <https://doi.org/10.1016/j.canlet.2019.07.010>.
- [56] K. Jin, N.B. Pandey, A.S. Popel, Crosstalk between stromal components and tumor cells of TNBC via secreted factors enhances tumor growth and metastasis, *Oncotarget* 8 (2017) 60210–60222, <https://doi.org/10.18632/oncotarget.19417>.
- [57] T.A. Martin, A. Goyal, G. Watkins, W.G. Jiang, Expression of the transcription factors snail, slug, and twist and their clinical significance in human breast cancer, *Ann. Surg. Oncol.* 12 (2005) 488–496, <https://doi.org/10.1245/ASO.2005.04.010>.
- [58] B. Weigelt, J.L. Peterse, L.J.V. Veer, Breast cancer metastasis: markers and models, *Nat. Rev. Cancer* 5 (2005) 591–602, <https://doi.org/10.1038/nrc1670>.
- [59] A.J. Gooding, W.P. Schiemann, Epithelial-mesenchymal transition programs and cancer stem cell phenotypes: mediators of breast cancer therapy resistance, *Mol. Cancer Res.* 18 (2020) 1257–1270, <https://doi.org/10.1158/1541-7786.MCR-20-0067>.
- [60] Y. Yu, C.H. Xiao, L.D. Tan, Q.S. Wang, X.Q. Li, Y.M. Feng, Cancer-associated fibroblasts induce epithelial-mesenchymal transition of breast cancer cells through paracrine TGF- β signalling, *Br. J. Cancer* 110 (2014) 724–732, <https://doi.org/10.1038/bjc.2013.768>.
- [61] M. Huang, M. Fu, J. Wang, C. Xia, H. Zhang, Y. Xiong, J. He, J. Liu, B. Liu, S. Pan, F. Liu, TGF- β 1-activated cancer-associated fibroblasts promote breast cancer invasion, metastasis and epithelial-mesenchymal transition by autophagy or overexpression of FAP- α , *Biochem. Pharmacol.* 188 (2021), 114527, <https://doi.org/10.1016/j.bcp.2021.114527>.
- [62] T.M. Casey, J. Eneman, A. Crocker, J. White, J. Tessitore, M. Stanley, S. Harlow, J. Y. Bunn, D. Weaver, H. Muss, K. Plaut, Cancer associated fibroblasts stimulated by transforming growth factor beta1 (TGF- β 1) increase invasion rate of tumor cells: a population study, *Breast Cancer Res. Treat.* 110 (2008) 39–49, <https://doi.org/10.1007/s10549-007-9684-7>.
- [63] M. Yamashita, T. Ogawa, X. Zhang, N. Hanamura, Y. Kashikura, M. Takamura, M. Yoneda, T. Shiraiishi, Role of stromal myofibroblasts in invasive breast cancer: stromal expression of alpha-smooth muscle actin correlates with worse clinical

- outcome, *Breast Cancer* 19 (2012) 170–176, <https://doi.org/10.1007/s12282-010-0234-5>.
- [64] E.W. Thompson, S. Paik, N. Brüner, C.L. Sommers, G. Zugmaier, R. Clarke, T. B. Shima, J. Torri, S. Donahue, M.E. Lippman, G.R. Martin, R.B. Dickson, Association of increased basement membrane invasiveness with absence of estrogen receptor and expression of vimentin in human breast cancer cell lines, *J. Cell. Physiol.* 150 (1992) 534–544, <https://doi.org/10.1002/jcp.1041500314>.
- [65] K. Vuoriluoto, H. Haugen, S. Kiviluoto, J.P. Mpindi, J. Nevo, C. Gjerdrum, C. Tiron, J.B. Lorens, J. Ivaska, Vimentin regulates EMT induction by Slug and oncogenic H-Ras and migration by governing Axl expression in breast cancer, *Oncogene* 30 (2011) 1436–1448, <https://doi.org/10.1038/ncr.2010.509>.
- [66] M.H.S. Chen, G.W.-C. Yip, G.M.K. Tse, T. Moriya, P.C.W. Lui, M.L. Zin, B.H. Bay, P. H. Tan, Expression of basal keratins and vimentin in breast cancers of young women correlates with adverse pathologic parameters, *Mod. Pathol.* 21 (2008) 1183–1191, <https://doi.org/10.1038/modpathol.2008.90>.
- [67] H. Sugimoto, T.M. Mundel, M.W. Kieran, R. Kalluri, Identification of fibroblast heterogeneity in the tumor microenvironment, *Cancer Biol. Ther.* 5 (2006) 1640–1646, <https://doi.org/10.4161/cbt.5.12.3354>.
- [68] H.M. DeLisser, M. Christofidou-Solomidou, R.M. Strieter, M.D. Burdick, C. S. Robinson, R.S. Wexler, J.S. Kerr, C. Garlanda, J.R. Merwin, J.A. Madri, S. M. Albelda, Involvement of endothelial PECAM-1/CD31 in angiogenesis, *Am. J. Pathol.* 151 (1997).
- [69] J.K. Singh, B.M. Simões, S.J. Howell, G. Farnie, R.B. Clarke, Recent advances reveal IL-8 signaling as a potential key to targeting breast cancer stem cells, *Breast Cancer Res.* 15 (2013) 210, <https://doi.org/10.1186/bcr3436>.
- [70] C. Ginestier, S. Liu, M.E. Diebel, H. Korkaya, M. Luo, M. Brown, J. Wicinski, O. Cabaud, E. Charafe-Jauffret, D. Birnbaum, J.L. Guan, G. Dontu, M.S. Wicha, CXCR1 blockade selectively targets human breast cancer stem cells in vitro and in xenografts, *J. Clin. Invest.* 120 (2010) 485–497, <https://doi.org/10.1172/JCI39397>.
- [71] Y. Lin, R.P. Huang, L. Chen, S. Li, Q. Shi, C. Jordan, R.P. Huang, Identification of interleukin-8 as estrogen receptor-regulated factor involved in breast cancer invasion and angiogenesis by protein arrays, *Int. J. Cancer* 109 (2004), <https://doi.org/10.1002/ijc.11724>.
- [72] L. Wang, C. Tang, H. Cao, K. Li, X. Pang, L. Zhong, W. Dang, H. Tang, Y. Huang, L. Wei, M. Su, T. Chen, Activation of IL-8 via PI3K/AKT-dependent pathway is involved in leptin-mediated epithelial-mesenchymal transition in human breast cancer cells, *Cancer Biol. Ther.* 16 (2015) 1220–1230, <https://doi.org/10.1080/15384047.2015.1056409>.
- [73] K.M. Lee, K. Nam, S. Oh, J. Lim, R.K. Kim, D. Shim, J.H. Choi, S.J. Lee, J.H. Yu, J. W. Lee, S.H. Ahn, I. Shin, ECM1 regulates tumor metastasis and CSC-like property through stabilization of β -catenin, *Oncogene* 34 (2015) 6055–6065, <https://doi.org/10.1038/ncr.2015.54>.
- [74] P. Gómez-Contreras, J.M. Ramiro-Díaz, A. Sierra, C. Stipp, F.E. Domann, R. J. Weigel, G. Lal, Extracellular matrix 1 (ECM1) regulates the actin cytoskeletal architecture of aggressive breast cancer cells in part via S100A4 and Rho-family GTPases, *Clin. Exp. Metastasis* 34 (2017) 37–49, <https://doi.org/10.1007/s10585-016-9827-5>.
- [75] C. Thomas, W. Henry, B.G. Cuiffo, A.Y. Collmann, E. Marangoni, V. Benhamo, M. K. Bhasin, C. Fan, L. Fuhrmann, A.S. Baldwin, C. Perou, A. Vincent-Salomon, A. Toker, A.E. Karnoub, Pentraxin-3 is a PI3K signaling target that promotes stem cell-like traits in basal-like breast cancers, *Sci. Signal.* 10 (2017) eaah4674, <https://doi.org/10.1126/scisignal.aah4674>.
- [76] X. Su, Y. Xu, G.C. Fox, J. Xiang, K.A. Kwakwa, J.L. Davis, J.I. Belle, W.-C. Lee, W. H. Wong, F. Fontana, L.F. Hernandez-Aya, T. Kobayashi, H.M. Tomasson, J. Su, S. J. Bakewell, S.A. Stewart, C. Egbulefu, P. Karmakar, M.A. Meyer, D.J. Veis, D. G. DeNardo, G.M. Lanza, S. Achilefu, K.N. Weillbaecher, Breast cancer-derived GM-CSF regulates arginase 1 in myeloid cells to promote an immunosuppressive microenvironment, *J. Clin. Invest.* 131 (2021), e145296, <https://doi.org/10.1172/jci145296>.
- [77] H. Li, L. Zhou, J. Zhou, Q. Li, Q. Ji, Underlying mechanisms and drug intervention strategies for the tumour microenvironment, *J. Exp. Clin. Cancer Res.* 40 (2021) 97, <https://doi.org/10.1186/s13046-021-01893-y>.
- [78] C. Kim, R. Gao, E. Sei, R. Brandt, J. Hartman, T. Hatschek, N. Crosetto, T. Foukakis, N.E. Navin, Chemoresistance evolution in triple-negative breast cancer delineated by single-cell sequencing, *Cell* 173 (2018) 879–893.e13, <https://doi.org/10.1016/j.cell.2018.03.041>.